View metadata, citation and similar papers at core.ac.uk

brought to you by CORE

provided by DSpace@MIT

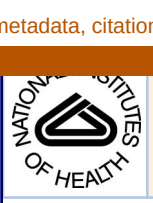

NIH Public Access
Author Manuscript
Cytometry A. Author manuscript; available in PMC 2015 July 01.

Published in final edited form as:
Cytometry A. 2015 January ; 87(1): 49–60. doi:10.1002/cyto.a.22584.

Three-Dimensional Image Cytometer Based on Widefield Structured Light Microscopy and High-Speed Remote Depth Scanning

Heejin Choi[1], **Dushan N. Wadduwage**[2,3], **Ting Yuan Tu**[2], **Paul Matsudaira**[3], and **Peter T. C. So**[1,2,4,5,★]

[1]Department of Mechanical Engineering, Massachusetts Institute of Technology, Cambridge, Massachusetts 02139

[2]Singapore MIT Alliance for Research and Technology, Singapore

[3]Department of Biological Science, National University of Singapore, Singapore

[4]Department of Biological Engineering, Massachusetts Institute of Technology, Cambridge, Massachusetts 02139

[5]Laser Biomedical Research Center, Massachusetts Institute of Technology, Cambridge, Massachusetts 02139

Abstract

A high throughput 3D image cytometer have been developed that improves imaging speed by an order of magnitude over current technologies. This imaging speed improvement was realized by combining several key components. First, a depth-resolved image can be rapidly generated using a structured light reconstruction algorithm that requires only two wide field images, one with uniform illumination and the other with structured illumination. Second, depth scanning is implemented using the high speed remote depth scanning. Finally, the large field of view, high NA objective lens and the high pixelation, high frame rate sCMOS camera enable high resolution, high sensitivity imaging of a large cell population. This system can image at 800 cell/sec in 3D at submicron resolution corresponding to imaging 1 million cells in 20 min. The statistical accuracy of this instrument is verified by quantitatively measuring rare cell populations with ratio ranging from 1:1 to $1:10^5$.

Key terms

3D image cytometry; structured light illumination; remote depth scanning; rare cell detection

Flow cytometry allows statistical analysis of a large population of cells (1). Flow cytometry is particularly powerful for characterizing the biochemical states of individual cells, such as whether particular proteins are expressed, based on fluorometric assays. The key strength of flow cytometry is speed that can routinely process 10,000 cell/sec; processing speed up to

© 2014 International Society for Advancement of Cytometry

Correspondence to: Peter T. C. So, 500 Technology Sq, NE47-279, Cambridge, MA 02139, USA. ptso@mit.edu.

NIH-PA Author Manuscript

NIH-PA Author Manuscript

NIH-PA Author Manuscript

NIH-PA Author Manuscript

NIH-PA Author Manuscript

NIH-PA Author Manuscript

100,000 cell/sec has also been demonstrated (2). A drawback of flow cytometry is that it provides little morphological information to more fully determine the phenotype of individual cells. Image cytometry was developed to address this need by performing high content assays providing both rich morphological and biochemical information (3–8). The increased information content is traded-off with reduced speed; image cytometry typically has throughput several orders of magnitude slower than flow cytometry. Image cytometry has found numerous applications in biology and pharmacology. As demonstrated by Bakal et al. morphological analysis of cell shape allows association of protein expression with mechanistic steps of cell migration (4). Perlman et al. have first shown that morphological responses of cells allow the classification of drugs and to identify mechanisms of new drugs (7).

A number of 2D image cytometers have been introduced with different instrument complexity and performance (9). Most of the commercially available systems deal with adherent cell types that are plated either on slide glasses or multi-well plates. For non-adherent cells, imaging flow cytometry has been developed to capture two dimensional images of floating cells as they are transported through the fluidic channel similar to the flow cytometry. The state of the art system can achieve 1,000 cell/sec imaging rate in bright field, dark field, and fluorescence simultaneously by imaging multiple cells with an extended depth of field of focus (10). Imaging flow cytometer has also been extended for in vivo detection of rare circulating cells (11). More recently, an exciting technique based on serial time-encoded in amplified ultrafast pulses has achieved frame rate up to 1 MHz for gray scale 2D images (12).

An important extension of image cytometry system is the addition of 3D resolution. 3D imaging capability can improve quantification of morphological features even in 2D cell culture environments. For example, 3D image cytometry can allow more accurate quantification of the number of DNA double stand breaks in cell nuclei that are often related to carcinogenic potential of cellular environment. DNA double strand breaks can be detected by immunofluorescent labeling of proteins such as H2AX (13). Double strand breaks associated with labeled H2AX appear as foci that are distributed in 3D. For nuclei with dense H2AX foci, foci on different depth but with overlapping lateral coordinates can be hard to distinguish with traditional 2D image cytometry. As another example, optically sectioned 3D imaging is required to study the stem cell differentiation process that is often co-cultured on a feeder cell layer (14). There are many other cases where 3D imaging can provide better quantification of cytometric features such as cell size, shape, and volume (15). Beyond 2D culture, 3D resolved images further enable studying of cells in tissue environment in situ. Since cells in tissue interact with and are regulated by their extracellular matrix, cells cultured in 3D matrix can better mimic the behavior of cells in tissue than cells cultured in 2D well plate or slide glass. For example, cell–matrix interaction has proven to be an important factor in determining the outcome of the nerve regeneration (16). In these 3D systems, image cytometer with 3D sectioning can better quantify cellular behavior in their native state. Today, most 3D image cytometers are based on the laser scanning microscopy such as confocal microscopy. Both spinning disk and line scanning confocal microscopy have been applied for frame rate improvement (17). 3D imaging based on multi-photon excitation has also been deployed for deeper imaging in more opaque tissue

NIH-PA Author Manuscript

NIH-PA Author Manuscript

NIH-PA Author Manuscript

specimen (18–20). The throughput in multiphoton imaging mode has been improved by scanning multiple foci in parallel or by using high speed polygonal mirror scanner (21). Recent advances in optical clearing technology have opened doors for studying whole organs on the single cellular level without sectioning (22–24).

In this article, we introduce a new implementation of high throughput 3D image cytometer based on structured light widefield (WF) fluorescence imaging coupled with high speed remote depth scanning. For almost confluent 2D cell cultures, this system can image at about 800 cell/sec in 3D at submicron resolution corresponding to imaging 1 million cells in 20 min. The throughput of this system is over an order of magnitude faster than state-of the-art commercial 3D image cytometers in terms of the number of resolvable pixel per second. The operation of this system is validated by performing high speed 3D imaging of 2D cell cultures and in thin 3D tissue sections. We have further demonstrated quantitative performance of this system in counting rare cells successfully detecting sub-population with dilution down to $1{:}10^5$.

Materials and Methods

High Throughput 3D Image Cytometer

Figure 1a shows the schematic layout of the 3D image cytometer. Three diode-pumped solid states lasers (CNI laser, Changchun, P.R. China) with emission wavelengths of 473 nm, 561 nm, and 660 nm, respectively, were used as light sources enabling the excitation of a broad range of fluorophores. The three laser outputs were combined into one collinear beam using the laser beam multiplexers (LM01-503-25, LM01-613-25, Semrock, Rochester, NY). Photobleaching was minimized by gating the excitation light with an optical shutter (Ch-61, EOPC, Ridge-wood, NY) synchronizing sample exposure with the integration period of the camera. The diffractive optical element (DOE) (DS-033-Q-Y-A, HOLO/OR, Rehovot, Israel) split the beam into +1 and −1 orders and minimized the power loss into 0th and higher orders (efficiency : 78% (473 nm), 80% (561 nm), 69% (660 nm)). Since the two beams generated by DOE reached the focal plane of the objective (W Plan-Apochromat ×20 1.0 N.A. water, Zeiss, Thornwood, NY) via a common path, interference resulted in a stable fringe pattern enabling structured light illumination (SLI) and produced structured illumination images (SI). Uniform illumination images (UI) were generated by blocking one of the excitation beam path with another optical shutter (Ch-61, EOPC). This fast optical shutter was triggered by an external Transistor-Transistor Logic (TTL) signal and allowed switching between UI and SI at speed up to 50 Hz. A quad-band dichroic mirror (FF410/504/582/669 -Di01-25×36, Semrock) was used to separate the excitation beam from the emitted fluorescence signal. A quad-band emission filter (FF01-440/521/607/700-25, Semrock) was placed right in front of the detector blocking any stray excitation light reflected from the intermediate optical elements. The z-scanning of the sample was performed remotely by first forming a perfect 3D image of the sample in the focal space of the remote focusing objective (CFI Plan Apochromat Lambda ×20 0.75 N.A. air, Nikon, Melville, NY) and then by scanning a mirror in the axial direction with a piezo actuator. The intermediate image formed at the focal plane of L_8 was relayed to the imaging detector after ×1.5 magnification. Up to 40 axial planes for both SI and UI can be imaged in one second

NIH-PA Author Manuscript

NIH-PA Author Manuscript

NIH-PA Author Manuscript

with this implementation. Different color channels can be selected by a filter wheel with three band pass filters (FF01-520/35, FF01-609/54, FF01-692/40, Semrock). sCMOS camera (PCO.EDGE 5.5, PCO, Kelheim, Germany) recorded a field of view with size of 420 μm × 350 μm at maximum 100 frame per second at 2,560 × 2,160 pixelation. When the bit depth of a pixel was 16 bit, the total data rate was ~1 GB/sec. Since the writing speeds of the currently available hard drives, including solid state ones, were limited to about 400 MB/sec, multiple hard drives were set up in a RAID 0 configuration to record the data in parallel which effectively increased the writing speed and storage capacity. Data acquisition followed a typical sequence. For a given field of view, a *z* stack of SI images were first acquired and a stack of UI images were acquired by blocking one illumination beam with the fast shutter. A fast motorized stage (SCAN IM 120×100-2 mm, Marzhauser, Wetzlar, Germany) then translated the sample to the next field of view with settling time below 100 msec. Afterward, the same data acquisition sequence was repeated. The data acquisition procedures were fully automated according to the timing diagram as shown in Figure 1b and controlled by the custom-made control software written in C# programming language.

Structured Light Illumination for Depth-Resolved Widefield Imaging

Many SLI have been developed to select a particular imaging plane and to reject out-of-focus background using a standard wide-field fluorescence microscope (25,26). Of these methods, one effective approach we adapted is termed “HiLo microscopy” which generates an optically sectioned image by post-processing using only one UI and one SI (26). The HiLo algorithm is based on an assumption that 2D image can be divided into low lateral frequency and high lateral frequency contents. Since the high lateral frequency contents always have depth resolution by the nature of the incoherent wide-field point spread function (PSF), the goal of using SLI is to encode the in-focus low frequency contents, especially the zero lateral frequency component, with high frequency SLI. More specifically, the in-focused high frequency contents are extracted by high-pass filtering UI with a Gaussian shaped high-pass filter. The in-focus low frequency contents are extracted by low-pass filtering the absolute of SI after subtracting it from UI. The cutoff frequency of the Gaussian filter is determined by the sinusoidal spatial frequency of the structured illumination. Subsequently, the optically sectioned image is obtained by combining these two filtered images with an adjustable scalar factor so that the transition from low to high frequencies occur smoothly (27). HiLo microscopy has been widely used in the context of the background rejection for light-sheet microscopy (27,28), temporally focused WF two photon microscopy (29), and depth-resolved microrheology (30). Comparing HiLo approach with other structured light methods, most other structured light methods require taking more images. For example, phase shifting SLI using three images has been implemented in commercial 3D image cytometer (31). Further, the 3D reconstruction fidelity of phase shifting SLI depends on phase shifting accuracy that is often limited by actuation speed rending this approach less compatible with high throughput cytometry. In our implementation of HiLo SLI, switching between SI and UI can be performed in high speed by just shuttering one of the two beams with a fast optical shutter without the need for any precise actuation. In addition, HiLo method is insensitive to the motion artifact of a sample since the precise phase control is not required. Figure 2 shows one example how the HiLo method can be used for rejecting the background signal. The fringe pattern projected on the

NIH-PA Author Manuscript

NIH-PA Author Manuscript

NIH-PA Author Manuscript

in-focused part of the sample is visible as shown in Figure 2b. HiLo processing removed the common background from out-of-focal regions and produced clearer image as shown in Figure 2c.

Axial Resolution of the SLI Measured with a Thin Rhodamine Solution

Theoretical axial resolution of SLI can be estimated using the defocused 2D optical transfer function (OTF) derived by Stokseth (32).

$$C(u, m)=f(m)\left\{\frac{2J_1(um[1-m/2])}{um[1-m/2]}\right\} \quad (1)$$

where $f(m) = 1 - 0.69m + 0.076m^2 + 0.043m^3$, m is the normalized fringe frequency and is related to the real fringe period T_g via $m = \lambda/(T_g \text{ NA})$, NA = $n \sin(\alpha)$ and u is the normalized defocus and is related to the actual defocus z via $u = 4kzn \sin^2(\alpha/2)$, $k = 2\pi/\lambda$. In incoherent detection, OTF represents the contrast of the fringe detected at the image plane and is equivalent to the signal generated when a thin sheet of fluorescence is scanned through the focus. Ideally, the best optical sectioning is achieved when the normalized fringe frequency comes close to unity (33). However, as the fringe frequency is increased the modulation depth is reduced which in turn reduces the signal-to-noise ratio.

As a demonstration of depth resolution of this approach, we translated a thin film of Rhoadmine solution through the focal plane. A florescent solution was prepared by first dissolving Rhodamine power (Rhodamine 6G, Sigma-Aldrich, St. Louis, MO) in alcohol and diluted to 300 μM concentration. Then, a drop of Rhodamine solution was placed on a slide glass and covered with a cover slip and squeezed to form a meniscus around the edge of the cover slip. The thickness of film was estimated from the ratio of the known volume of the drop of Rhodamine solution and the area of the coverslip; the target thickness should be less than the theoretical axial resolution of the optical system. Figure 3 shows the radially integrated fluorescence intensity at each depth in the vicinity of the focal plane of the objective for this thin sheet of fluorescent solution obtained with WF and SLI imaging, respectively. In case of WF imaging, the integrated fluorescence from each z plane was constant, which implies WF did not provide depth information for an object with zero lateral spatial frequency. This is caused by the “missing cone” effect of the OTF in WF fluorescence microscopy where there is no frequency support for the zero lateral frequency component. Practically, this means there is no discrimination against out-of-focus background resulting in significant decrease of the signal-to-background ratio. In confocal microscopy, the pinhole conjugated to the focal point filters out this background. In SLI, the SI acts analogously as a virtual, digital pinhole to filter out, computationally, the low frequency out-of-focus background beyond the depth-of-field of the objective. For fringe period of 1.3 μm, Eq. (1) predicts that the axial intensity distribution has a full-width-at-half-maximum (FWHM) of 1.28 μm in satisfactorily agreement with experimental value of 1.84 ± 0.05 μm.

NIH-PA Author Manuscript

NIH-PA Author Manuscript

NIH-PA Author Manuscript

High Speed Remote Depth Scanning

For volumetric imaging, the microscope objective is typically translated in the axial direction using a piezo-scanner. However, direct objective scanning is relatively slow because of the large inertia of the objective. Although volumetric imaging has been demonstrated by resonantly driving the objective piezo scanner at 10 Hz (34), the resulting vibration can transmit through the immersion medium and may induce motion artifacts in biological specimens. One way to improve the scanning speed without sample disturbance is to form a perfect 3D image of an object remotely and sequentially scanning the remotely formed 3D image in the axial direction with a small light-weight mirror driven by a piezo actuator (35). Perfect 3D imaging can be achieved by designing the imaging system such that it satisfies both the sine and the Herschel condition. As a consequence of these constraints, the lateral and the longitudinal magnifications of the imaging system becomes equal to the ratio of the immersion media refractive indices of the object and the image space (36). As proposed by Botcherby et al. (35), the perfect 3D imaging system can be constructed by ensuring that the intermediate optical elements satisfy Eq. (2) which can be derived from the perfect imaging condition.

$$\frac{f_2}{f_1}=\frac{n_2 M_1 F_2}{n_1 M_2 F_1} \quad (2)$$

where f_1 and f_2 are the focal length of the imaging and the remote focusing objective respectively. n_1 and n_2 are the refractive index of the immersion medium in object and image space respectively. M_1 and M_2 are the magnification of the objectives. F_1 and F_2 are the nominal focal length of the objectives.

Practically, the pupil plane of the imaging objective (W Plan-Apochromat ×20 1.0 N.A. water, Zeiss) should be imaged onto the pupil plane of the remote focusing objective (CFI Plan Apochromat Lambda ×20 0.75 N.A. air, Nikon) by a 4-f system consisting of a Zeiss tube lens with 164.5 mm focal length (58–452, Edmund Optics, Barrington, NJ) and an achromatic doublet with 150 mm focal length (AC504-150-A, Thorlabs, Newton, NJ) such that the phase distortion induced by the imaging objective can be cancelled out by the equal amount of negative phase distortion induced by the remote focusing objective. This arrangement should result in a distortion-free 3D image to be formed with isotropic magnification in all directions (37). The axial scanning was performed by moving the mirror (NT68-321, Edmund Optics) attached to the piezo actuator (P-830.10, Physik Instrumente, Auburn, MA). The travel range of the current piezo actuator was 15 μm, which corresponds to 22.5 μm scanning range in the object space taking into account the magnification ratio. Since an air immersion objective (ROBJ, see Fig. 1) was chosen for remote focusing, very minimal mechanical disturbance was induced even for high speed scanning. Since the ROBJ was designed for imaging through a 170 μm coverslip, a coverslip was placed in between ROBJ and the remote focusing mirror to minimize spherical aberration. To improve the detection efficiency of the unpolarized fluorescence emission light, a $\lambda/4$ plate (2-APW-L/4-018A, Altechna, Vilnius, Lithuania) and a broadband polarizing cube beamsplitter (10FC16PB.3, New-port, Irvine, CA) were used as shown in Figure 1a, which can collect up to 50% of the unpolarized emission light. However, since excitation light is polarized and

NIH-PA Author Manuscript

NIH-PA Author Manuscript

NIH-PA Author Manuscript

emission dipole is often aligned with excitation dipole, there are emission light losses by a polarizing beam splitter but is often much less than 50%.

The PSF of the remote focusing system was measured by imaging 0.5 μm fluorescent beads immersed in 2% Agarose gel at axially different locations through the focal region of the imaging objective (OBJ, see Fig. 1). After a bead was placed at the focal plane of the objective, the position of the bead relative to the focal plane of the objective was varied by moving the objective manually which was mounted on the micrometer driven translation stage (SM1Z, Thorlabs). The positive direction corresponded to the objective moving away from the bead and the negative direction corresponded to the objective moving closer to the bead. At each position of the objective, the remote focusing mirror was scanned axially for a uniformly illuminated excitation beam to record the full diffraction pattern of a single bead. Figure 4 shows the PSFs from −100 μm to 100 μm at 20 μm interval. Slight asymmetry was observed in the PSF of the bead located at the focal plane. We further observed that as the bead was translated away from the focal plane, its PSF was further elongated consistently. Both observations were consistent with the presence of spherical aberration. This aberration may partly originate from the indices mismatch between the objective immersion liquid and the agarose gel surrounding the bead. This aberration may also partly originate from the incomplete phase distortion cancellation between the imaging objective and the remote focusing objective. Finally, since the remote focusing theory was based on the linear approximation with the point source near the focal plane, deviation from linearity may also partly account for the increasing PSF distortion away from the focal plane (37).

Results and Discussion

Extracting 3D Morphological Information from Thin Tissue Sections and 2D Cell Cultures

3D resolved imaging capability of this cytometer was demonstrated in biological specimens. Figure 5 shows the 3D image stacks of a mouse kidney section (F-24630, Molecular Probe, Grand Island, NY) obtained with the uniform illumination (Fig. 5a) and the same section after the HiLo processing (Fig. 5b). Elements of the glomeruli and convoluted tubules labeled with Alexa Fluor® 488 wheat germ agglutinin were excited with the 473nm laser line and the emission light was detected with 520 nm/35 nm band pass filter (FF01-520/35, Semrock). The filamentous actin prevalent in glomeruli and the brush border labeled with red-fluorescent Alexa Fluor 568 phalloidin was excited with the 561 nm laser line and the emission light was detected with the 609 nm/54 nm band pass filter (FF01-609/54, Semrock). The out-of-focus background that blurs images was removed in the HiLo processed images and consequently the contrast was improved.

High resolution subcellular organelle features can also be quantified. Morphological features such as nuclear size, perimeter of the cytoplasm, and 3D distribution of the protein can be extracted and statistically processed to provide morphological context caused by physiological changes. As shown in Figure 6a, the 3D map of the mitochondria can be measured to study the metabolic states of the cells. As another example, high throughput 3D image cytometer was used in an image informatics to study transforming growth factor beta (TGFβ) signaling in determining fibroblast-myofibroblast differentiation in collagen scaffold matrix. Figure 6b shows the fibroblast activated by TGFβ resulting in a cascade of SMAD

NIH-PA Author Manuscript

NIH-PA Author Manuscript

NIH-PA Author Manuscript

protein signaling that consequently resulted in higher expression of α-smooth actin, abundant stress fiber formation, and an increase in cell-scaffold traction.

The developed 3D image cytometer can also acquire a large sample size at submicron resolution where the size limit is only constrained by the scanning range of the motorized stage. Figure 7 shows a section of the whole mouse kidney that was imaged with 473 nm laser line and 520 nm/35 nm band pass filter. Total 16 × 16 field of views (FOVs) were stitched together in the post processing. This data clearly demonstrates that this image cytometer can maintain high spatial resolution during large field of view imaging.

Rare Cell Detection in 2D Cell Culture

The quantitative performance of this image cytometer was further characterized by counting rare cell subpopulations in culture (21). The ability to detect a rare cell can potentially find applications in cancer diagnosis. For example, there are about 1–10 circulating tumor cell (CTC) out of 1 million white blood cells (38). As the cancer progresses, the number of CTC in the blood stream increases. The ability to detect CTC in early stage of cancer requires a high throughput system that can screen out CTC in a short time scale.

2D cell culture preparation—A549 human alveolar adeno-carcinoma cells transfected with histone H2B-mCherry cDNA for nuclear staining were maintained in two T75 flasks (Nun-clon Δ Surface) in Dulbecco's modified Eagle medium (Gibco, Invitrogen, Grand Island, NY) supplemented with 10% fetal bovine serum (Gibco, Invitrogen) and 1% penicillin–streptomycin. Puromycin 0.01% was added for the selection of mCherry-expressing cells with the medium change every 36–48 h. To prepare rare cells with cytoplasm staining prior to the imaging, one of the flasks of the grown cells were labeled with 5-chloromethylfluorescein diacetate (CMFDA Cell Tracker ™ Green, Invitrogen, Grand Island, NY) and incubated for 20 min, and then replaced with serum free culture medium for another 20 min. For passage, cells at 70–80% confluency were detached from both flasks by treating with 0.05% trypsin–ethylenedinitriletetraacetic acid (Trypsin–EDTA) at 37°C in an incubator for 3 min. Medium was then added to inhibit the enzymatic reaction of Trypsin–EDTA. Sub-culture seeding density was kept at 2–3 × 10^4 cells/ml. In one group of cells, nuclei were expressing with mCherry with emission peak at 560 nm. In the other group of cells, cytoplasm was labeled with CMFDA with emission peak at 520 nm in addition to the nuclei staining. The latter group of cells with both nuclei and cytoplasm labeling played the role of the rare cells. The two groups of cells, detached using the aforementioned procedure for passage, were re-suspended to two cell suspensions of 10^4 cells/μl. Imaging samples were prepared using the two cell suspensions with a range of mixing ratios: 1:1, 1:10, 1:10^2, 1:10^3, 10^4, and 1:10^5. The mixed populations of cells were plated in a 8-well chamber and incubated for about 6 h, with each well chamber containing about 5 × 10^4 cells. It should be noted that at least 20 rare cells were used to generate the specified ratios to achieve reasonable statistical accuracy. For example, in the sample of 1:10^5 ratio, the total number of cells was 2 million and the number of rare cells was about 20. All cell samples were fixed using 4% paraformaldehyde (PFA) and maintained in phosphate buffered saline (PBS) to be used for long-term imaging.

NIH-PA Author Manuscript

NIH-PA Author Manuscript

NIH-PA Author Manuscript

Data acquisition and analysis—The typical image acquisition procedure of the 3D cell cytometer was as follows. For a single field of view with size of 420 μm × 350 μm, SI image stack was first acquired with the SLI generated by the interference of the two beams with shutter (OS_2) open and then for the same FOV the UI image stack was acquired with the uniform illumination by blocking one of the beam with shutter (OS_2) closed. The motorized stage then translated the sample to the next FOV and the same sequence for acquiring UI and SI image stack was repeated until the whole sample area was covered. For the multi-color imaging, the above procedure was repeated for each detection color selected by the band pass filter wheel. To maintain the immersion medium in place during the stage scanning, a water chamber was constructed around the imaging objective lens and filled up with immersion medium.

A representative 3D image of rare cell sample at 1:1 mixing ratio is shown in Figure 8. For the rare cell detection experiment, the prepared samples of two group of cells mixed at different ratios were imaged with uniform illumination. Before starting the image acquisition, the tilting of the sample holder was adjusted to ensure that the whole imaging area remained in focus over the scanning range of the motorized stage. Cytoplasm labeled with Cell Tracker Green was excited with the 473 nm laser line and the emission light was imaged with 520 nm/35 nm band pass filter (FF01-520/35, Semrock). Nucleus labeled with m-Cherry was excited with the 561 nm laser line and the emission light was imaged with the 609 nm/54 nm band pass filter (FF01-609/54, Semrock). Figure 9 shows the representative image of $1:10^4$ sample. The acquired image was processed to count the number of cell in each population. The cell counting algorithm was implemented in MATLAB (MathWorks, Natick, MA). The image processing algorithm requires fairly extensive discussion and is included as an Appendix. Figure 10 shows the rare cell counting results. The expected ratio and the corresponding measured ratio is plotted in log scale in both *x* and *y* axis. The accurate correlation between the expected ratio and the measured ratio can be confirmed from the slope (0.9299) and the goodness-of-fit ($R^2 = 0.9964$) of the linear regression line. This result demonstrates the capability of the developed system for detecting rare cell populations down to a ratio of $1:10^5$.

Conclusions

This paper presents a high throughput 3D image cytometer dedicated for cell cultures and thin tissue sections based on the optically sectioned SLI WF fluorescence imaging and the high speed remote depth scanning. These features combined the use of high NA, large FOV objective and large pixilation, high frame rate sCMOS camera resulting in a highly optimized 3D image cytometer. The developed system enables image cytometry investigation to study cultured cell morphologies with statistical significance comparable to the flow cytometer. For a highly confluent cells, this system can image at about 800 cell/sec in 3D at submicron resolution. Compared to the commercially available high throughput, high contents 3D cytometer, that are either based on confocal microscopy or three-phase SLI microscopy, the developed system enables an order of magnitude faster throughput in terms of the number of resolvable point per second. The statistical rare cell detection accuracy of this instrument is verified by quantifying populations down to $1:10^5$.

NIH-PA Author Manuscript

NIH-PA Author Manuscript

NIH-PA Author Manuscript

Acknowledgments

Grant sponsor: NIH, Grant numbers: 9P41EB015871-26A1, 5R01EY017656-02, 5R01 NS051320, 4R44EB012415-02

Grant sponsor: NSF, Grant number: CBET-0939511

Grant sponsors: Singapore-MIT Alliance 2, MIT SkolTech initiative, Hamamatsu Corp., Koch Institute for Integrative Cancer Research Bridge Project Initiative

Literature Cited

1. Pedreira CE, Costa ES, Lecrevisse Q, van Dongen JJM, Orfao A. Overview of clinical flow cytometry data analysis: Recent advances and future challenges. Trends Biotechnol. 2013; 31:415–425. [PubMed: 23746659]
2. Leary JF, Schmidt DF, Gram JG, Mclaughlin SR, Torre CD, Burde S. High-speed flow cytometric analysis and sorting of human fetal cells from maternal blood for molecular characterization. Ann NY Acad Sci. 1994; 731:138–141. [PubMed: 7524388]
3. Alabi CA, Love KT, Sahay G, Yin H, Luly KM, Langer R, Anderson DG. Multiparametric approach for the evaluation of lipid nanoparticles for siRNA delivery. Proc Natl Acad Sci USA. 2013; 110:12881–12886. [PubMed: 23882076]
4. Bakal C, Aach J, Church G, Perrimon N. Quantitative morphological signatures define local signaling networks regulating cell morphology. Science. 2007; 316:1753–1756. [PubMed: 17588932]
5. Cappella P, Gasparri F. Highly multiplexed phenotypic imaging for cell proliferation studies. J Biomol Screen. 2014; 19:145–157. [PubMed: 23896684]
6. Echeverria V, Meyvantsson I, Skoien A, Worzella T, Lamers C, Hayes S. An automated high-content assay for tumor cell migration through 3-dimensional matrices. J Biomol Screen. 2010; 15:1144–1151. [PubMed: 20930216]
7. Perlman ZE, Slack MD, Feng Y, Mitchison TJ, Wu LF, Altschuler SJ. Multidimensional drug profiling by automated microscopy. Science. 2004; 306:1194–1198. [PubMed: 15539606]
8. Shibai-Ogata A, Tahara H, Yamamoto Y, Fujita M, Satoh H, Yuasa A, Hioki T, Kasahara T. An automated new technique for scoring the in vivo micronucleus assay with image analysis. Mutagenesis. 2014; 29:63–71.
9. Taylor, DL.; Haskins, JR.; Giuliano, K. High Content Screening: A Powerful Approach to Systems Cell Biology and Drug Discovery. Vol. 356. Totowa, NJ: Humana Press; 2007.
10. Basiji DA, Ortyn WE, Liang L, Venkatachalam V, Morrissey P. Cellular image analysis and imaging by flow cytometry. Clin Lab Med. 2007; 27:653–669. [PubMed: 17658411]
11. Lee H, Alt C, Pitsillides CM, Puoris'haag M, Lin CP. In vivo imaging flow cytometer. Opt Express. 2006; 14:7789–7800. [PubMed: 19529148]
12. Goda K, Tsia KK, Jalali B. Serial time-encoded amplified imaging for real-time observation of fast dynamic phenomena. Nature. 2009; 458:1145–1150. [PubMed: 19407796]
13. Bonner WM, Redon CE, Dickey JS, Nakamura AJ, Sedelnikova OA, Solier S, Pommier Y. OPINION gamma H2AX and cancer. Nat Rev Cancer. 2008; 8:957–967. [PubMed: 19005492]
14. Soto-Gutierrez A, Navarro-Alvarez N, Zhao D, Rivas-Carrillo JD, Lebkowski J, Tanaka N, Fox IJ, Kobayashi N. Differentiation of mouse embryonic stem cells to hepatocyte-like cells by co-culture with human liver nonparenchymal cell lines. Nat Protoc. 2007; 2:347–356. [PubMed: 17406596]
15. Kiehl TR, Shen D, Khattak SF, Li ZJ, Sharfstein ST. Observations of cell size dynamics under osmotic stress. Cytometry A. 2011; 79A:560–569. [PubMed: 21656664]
16. Tzeranis, DS. PhD thesis. Massachusetts Institute of Technology; 2013. Imaging Studies of Peripheral Nerve Regeneration Induced by Porous Collagen Biomaterials.
17. Mei E, Fomitchov PA, Graves R, Campion M. A line scanning confocal fluorescent microscope using a CMOS rolling shutter as an adjustable aperture. J Microsc Oxford. 2012; 247:269–276. [PubMed: 22906014]

NIH-PA Author Manuscript NIH-PA Author Manuscript NIH-PA Author Manuscript

18. Kwon HS, Nam YS, Wiktor-Brown DM, Engelward BP, So PTC. Quantitative morphometric measurements using site selective image cytometry of intact tissue. J R Soc Interface. 2009; 6:S45–S57. [PubMed: 19049958]
19. Ragan T, Kadiri LR, Venkataraju KU, Bahlmann K, Sutin J, Taranda J, Arganda-Carreras I, Kim Y, Seung HS, Osten P. Serial two-photon tomography for automated ex vivo mouse brain imaging. Nat Methods. 2012; 9:255–258. [PubMed: 22245809]
20. Ragan T, Sylvan JD, Kim KH, Huang H, Bahlmann K, Lee RT, So PTC. High-resolution whole organ imaging using two-photon tissue cytometry. J Biomed Opt. 2007; 12:014015. [PubMed: 17343490]
21. Kim KH, Ragan T, Previte MJR, Bahlmann K, Harley BA, Wiktor-Brown DA, Stitt MS, Hendricks CA, Almeida KH, Engelward BP, et al. Three-dimensional tissue cytometer based on high-speed multiphoton microscopy. Cytometry A. 2007; 71A:991–1002. [PubMed: 17929292]
22. Hama H, Kurokawa H, Kawano H, Ando R, Shimogori T, Noda H, Fukami K, Sakaue-Sawano A, Miyawaki A. Scale: A chemical approach for fluorescence imaging and reconstruction of transparent mouse brain. Nat Neurosci. 2011; 14:1481–1488. [PubMed: 21878933]
23. Chung K, Deisseroth K. CLARITY for mapping the nervous system. Nat Methods. 2013; 10:508–513. [PubMed: 23722210]
24. Ke MT, Fujimoto S, Imai T. SeeDB: A simple and morphology-preserving optical clearing agent for neuronal circuit reconstruction. Nat Neurosci. 2013; 16:1154–1161. [PubMed: 23792946]
25. Neil MAA, Juskaitis R, Wilson T. Method of obtaining optical sectioning by using structured light in a conventional microscope. Opt Lett. 1997; 22:1905–1907. [PubMed: 18188403]
26. Lim D, Chu KK, Mertz J. Wide-field fluorescence sectioning with hybrid speckle and uniform-illumination microscopy. Opt Lett. 2008; 33:1819–1821. [PubMed: 18709098]
27. Mertz J, Kim J. Scanning light-sheet microscopy in the whole mouse brain with HiLo background rejection. J Biomed Opt. 2010; 15:016027. [PubMed: 20210471]
28. Bhattacharya D, Singh VR, Zhi C, So PTC, Matsudaira P, Barbastathis G. Three dimensional HiLo-based structured illumination for a digital scanned laser sheet microscopy (DSLM) in thick tissue imaging. Opt Express. 2012; 20:27337–27347. [PubMed: 23262684]
29. Choi H, Yew EYS, Hallacoglu B, Fantini S, Sheppard CJR, So PTC. Improvement of axial resolution and contrast in temporally focused widefield two-photon microscopy with structured light illumination. Biomed Opt Express. 2013; 4:995–1005. [PubMed: 23847726]
30. Michaelson J, Choi HJ, So P, Huang HD. Depth-resolved cellular microrheology using HiLo microscopy. Biomed Opt Express. 2012; 3:1241–1255. [PubMed: 22741071]
31. Weigel A, Schild D, Zeug A. Resolution in the ApoTome and the confocal laser scanning microscope: Comparison. J Biomed Opt. 2009; 14:014022. [PubMed: 19256710]
32. Stokseth PA. Properties of a defocused optical system. J Opt Soc Am. 1969; 59:1314–1321.
33. Karadaglic D, Wilson T. Image formation in structured illumination wide-field fluorescence microscopy. Micron. 2008; 39:808–818. [PubMed: 18337108]
34. Gobel W, Kampa BM, Helmchen F. Imaging cellular network dynamics in three dimensions using fast 3D laser scanning. Nat Methods. 2007; 4:73–79. [PubMed: 17143280]
35. Botcherby EJ, Juskaitis R, Booth MJ, Wilson T. Aberration-free optical refocusing in high numerical aperture microscopy. Opt Lett. 2007; 32:2007–2009. [PubMed: 17632625]
36. Born, M.; Wolf, E. Principles of Optics. 7. London, UK: Pergamon; 1999.
37. Botcherby EJ, Juskaitis R, Booth MJ, Wilson T. An optical technique for remote focusing in microscopy. Opt Commun. 2008; 281:880–887.
38. Miller MC, Doyle GV, Terstappen LW. Significance of circulating tumor cells detected by the CellSearch system in patients with metastatic breast colorectal and prostate cancer. J Oncol. 2010; 2010:617421. [PubMed: 20016752]
39. Singh VR, Rajapakse JC, Yu H, So PTC. Intensity normalization of two-photon microscopy images for liver fibrosis analysis. Proc SPIE. 2011:7903.
40. Gonzalez, RC.; Woods, RE.; Eddins, SL. Digital Image Processing Using MATLAB. 2. Upper Saddle River, NJ: Pearson Prentice Hall; 2009.

NIH-PA Author Manuscript

NIH-PA Author Manuscript

NIH-PA Author Manuscript

41. Soille, P. Morphological Image Analysis: Principles and Applications. Berlin, NY: Springer-Verlag; 1999.
42. Zhang Y, Matuszewski BJ, Shark LK, Moore CJ. Medical image segmentation using new hybrid level-set method. Medivisj. 2008:71–76.
43. Meyer F. Topographic distance and watershed lines. Signal Process. 1994; 38:113–125.

Appendix: Image Processing Procedure

Flat-Field Correction

The raw images acquired by the cytometer system were generally affected by the field inequality of the illumination FOV caused by the non-uniform intensity distribution of the excitation laser beam profile. Therefore, B-spline based technique was employed to fit for the excitation pattern and normalize the intensity distribution over the FOV before image mosaicing. Since the high throughput imaging often involves sample with the length scale of on the order of tens of millimeters which corresponds to a 10^4 times of a FOV, a completely data driven approach was employed to determine the background as well as signal pattern. We used a combined additive and multiplicative model to normalize the FOV. First, the background was approximated by taking the minimum projection greater than a predefined noise level of the detector over all the images of the sample (I_{BG}). Second, the illumination pattern was approximated by the mean projection of the same image set after capping the pixels with photon count greater than a predefined threshold in order to account for the significantly brighter regions (I_S). Then, the flat-field correction was estimated for each image I (for each FOV) using Eq. (A.1).

$$I=\frac{I-IB_{\mathrm{BG}}}{IB_{\mathrm{S}}-IB_{\mathrm{BG}}} \quad \text{(A.1)}$$

where IB_{BG} is the 2D B-spline fitted to I_{BG} and IB_S is the 2D B-spline fitted to I_S.

Image Mosaicing

The flat field corrected images were then stitched together using a maximum cross correlation based algorithm (39) to generate an image mosaic for each sample. The images were first arranged in a 2D matrix according to the scan pattern of the motorized stage and the neighboring images were overlapped according to the extent of overlap introduced during image acquisition. Due to the limited accuracy of the stage positioning there were slight changes in the overlap in the different regions of the image mosaic. Hence for each boundary between two FOVs in the image matrix the size of overlap was changed in a sequence of steps in both X and Y directions in a predefined range and the cross correlation coefficient was calculated for each step. The XY position, which resulted in the maximum cross correlation coefficient, was chosen as the best overlap for the particular boundary between the particular FOVs. This procedure was repeated for all the boundaries between all the images (FOVs) in the mosaic to generate the final stitched image of the sample.

NIH-PA Author Manuscript
NIH-PA Author Manuscript
NIH-PA Author Manuscript

Segmentation and Cell Counting Algorithm

The cell counting algorithm was designed according to the labeling of the culture. All the cells contain the nucleus label and hence, it was used to detect and count the total number of cells in the sample. The rare cells containing the cytoplasm label were imaged in a separate channel and it was used in conjunction with the nucleus to separate the rare cells from the normal ones.

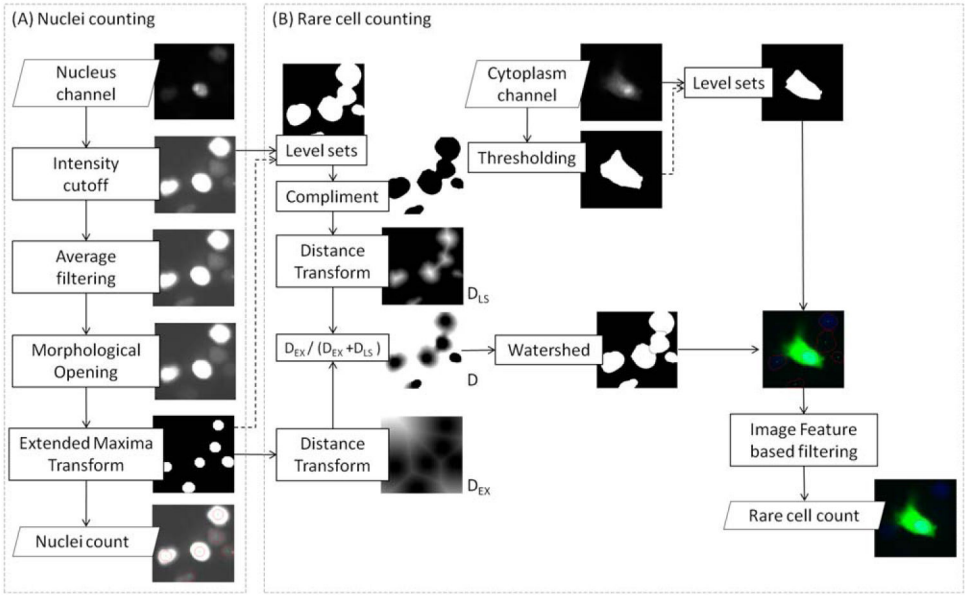

Figure A.1.
Cell counting pipeline: (**a**) nuclei counting, (**b**) rare cell counting. [Color figure can be viewed in the online issue, which is available at wileyonlinelibrary.com.]

The algorithm for nuclei segmentation and counting is as follows. The nuclei of the cells labeled using mCherry were exited using a 561 nm laser line and were imaged in one channel (nucleus channel). First, the stitched image of the nucleus channel was applied with a maximum cutoff intensity, i.e. all the pixels with greater photon count than the cutoff was assigned as the cutoff photon count. Second, the resulting image was spatially filtered using a circular averaging filter to smooth the image. Then, morphological opening (40) using a circular structuring element was applied on the image. These steps preprocess the original image to help identify local intensity peaks, which were used to count the number of nuclei in the sample. Then, the extended maxima transform, which was used to find local maxima on the *h*-maxima transform (41), was performed to identify the intensity peaks representing the nuclei. The number of connected components of the resulting binary image were counted to determine the number of nuclei, and hence the number of cells, in the sample. The nuclei counting pipeline is shown in Figure A.1a.

The algorithm for counting rare cell with cytoplasmic label is as follows. In order to count the number of cytoplasm labeled cells, the stitched image from the cytoplasm channel was first segmented using a predefined threshold and then morphological opening was performed

NIH-PA Author Manuscript

NIH-PA Author Manuscript

NIH-PA Author Manuscript

on the resulting binary image. This threshold was kept in a low enough value to include all the labeled cells since the counting accuracy should be high enough to detect the rare cell to normal cell ratio for all the samples with extreme mixing ratios such as $1:10^4$ and $1:10^5$. However this resulted in the inclusion of a significant fraction of false positives and hence further refining was necessary to separate true positives from false positives. Therefore, we characterized the true positive, i.e. cytoplasm and nucleus labeled cells using multiple image features of two channels. The image features used were, cell area (region enclosing from the cell boundary and is a measurement of cell volume), mean photon count of the cell area in cytoplasm channel, maximum photon count of the cell area in cytoplasm channel, the degree of overlap of the corresponding nucleus (nuclei for cell clusters), and the area ratio of the corresponding nucleus and the cytoplasm. Measuring the above features required proper cytoplasm and nucleus segmentation and therefore we applied a level-sets algorithm (42) to determine the correct segmentation boundary of the cytoplasm and the nucleus. The binary images from the nuclei counting and the cytoplasm thresholding were used as the starting points for the level-sets. For the clustered regions of the sample the above step determines the cluster boundary.

In order to separate the cells in the cell clusters we applied watershed (43) on the distance transform of a combined binary images resulting from the extended maxima transform and the level-sets of the nucleus channel according to the following equations (Fig. A1b)

$$D_{\mathrm{EX}} = \mathrm{distance\,Transform}(BW_{\mathrm{EX}})$$
$$D_{\mathrm{LS}} = \mathrm{distance\,Transform}(\mathrm{compliment}(BW_{\mathrm{LS}}))$$
$$D = \frac{D_{\mathrm{EX}}}{(D_{\mathrm{EX}} + D_{\mathrm{LS}})}$$
$$BW_{\mathrm{N}} = BW_{\mathrm{LS}} \& \mathrm{waterShed}(D)$$

Here D_{EX} and D_{LS} are respectively distance transforms of resulting binary image, BW_{EX} from nuclei counting step and resulting binary image and complement of BW_{LS} from nucleus segmentation using level sets. D is the combined distance image and BW_{N} is the final nuclei segmentation after cluster splitting using watershed on D. Finally, the correctly segmented nucleus and cytoplasm channels were used to measure the previously explained image features for each cytoplasm labeled segment and this multi-dimensional feature vector was thresholded to filter out the false positives and count the number of nuclei that includes label in the corresponding cytoplasm channel. The entire rare cell counting pipeline is shown in Figure A1b.

NIH-PA Author Manuscript

NIH-PA Author Manuscript

NIH-PA Author Manuscript

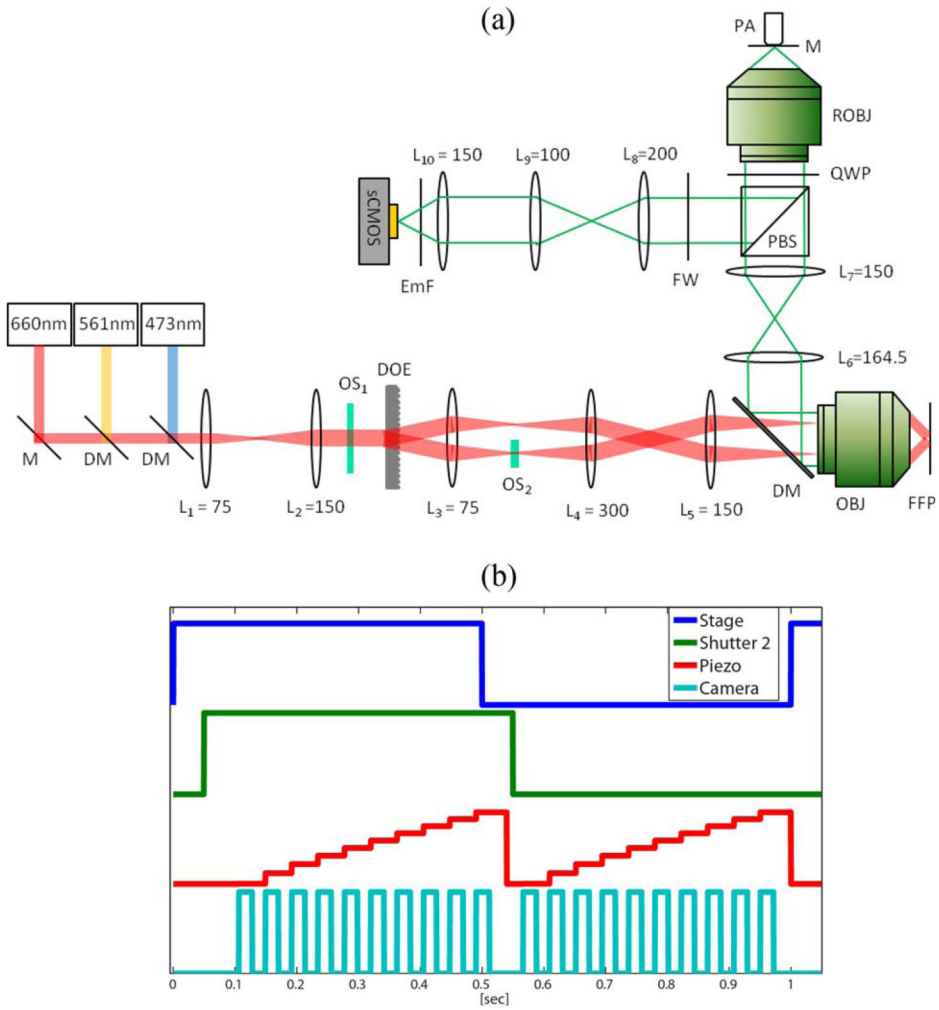

Figure 1.

(**a**) Schematic diagram of the high throughput 3D image cytometer. M: mirror, DM: dichroic mirror, DOE: diffractive optical element, OS_1: optical shutter for minimizing the photobleaching effect, OS_2: optical shutter for generating UI and SI, PBS: polarizing beam splitter cube, FW: filter wheel with three emission filter, QWP: quarter-wave plate, FW: bandpass filter wheel, EmF: emission filter, PA: piezo actuator, FFP: front focal plane, OBJ: imaging objective (Zeiss 20× Water NA1.0), ROBJ: remote focusing objective (Nikon 20× Air NA0.75). (**b**) Representative timing diagram for acquiring 10 images of both SI and UI per FOV. The motorized stage is triggered on the rising edge of TTL signal (blue). The shutter 2 opens for high TTL signal (green), which allows two beams from DOE to interfere at the focal plane for SLI and closes for low TTL signal, which blocks one of the beam from DOE to generate a UI. Piezo actuator moves at discrete step depending on the command voltage signal (red). The camera acquires a frame at each rising edge of the TTL signal (cyan) in synchrony with the piezo position. The camera triggering signal starts after 90 msec delay from the stage triggering signal due to the settling time of the stage. [Color figure can be viewed in the online issue, which is available at wileyonlinelibrary.com.]

NIH-PA Author Manuscript

NIH-PA Author Manuscript

NIH-PA Author Manuscript

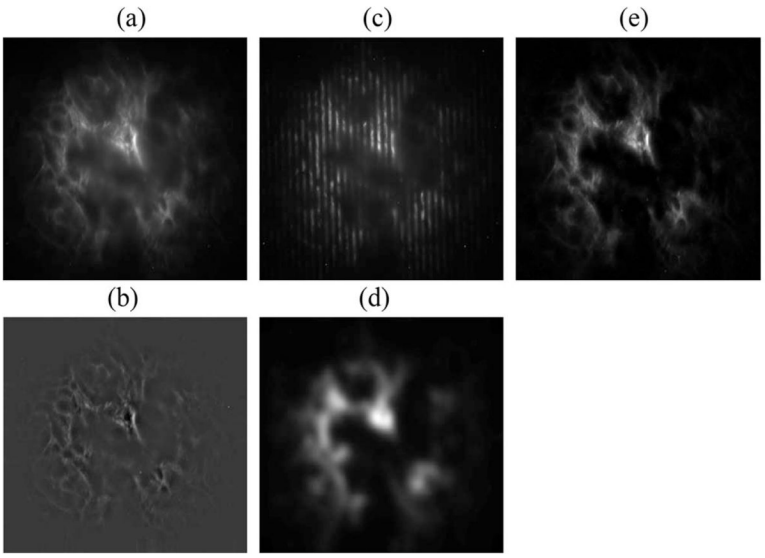

Figure 2.

Background rejection with HiLo algorithm. The sample is a section of the mouse kidney with 15 μm thickness. (**a**) Uniformly illuminated image (UI). (**b**) In-focused high frequency contents extracted by high-pass filtering UI with a Gaussian shaped high-pass filter. (**c**) Structurally illuminated image (SI). (**d**) In-focus low frequency contents extracted by low-pass filtering the absolute of SI after subtracting it from UI. (**e**) HiLo processed image obtained by combining (b) and (d) with an adjustable scalar factor.

NIH-PA Author Manuscript

NIH-PA Author Manuscript

NIH-PA Author Manuscript

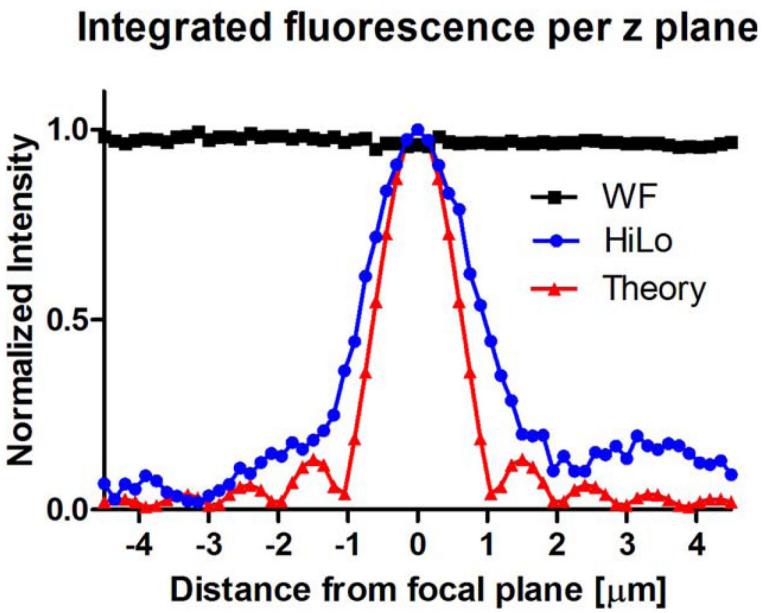

Figure 3.

Optical sectioning effect measured with thin sheet of Rhodamine solution. The integrated fluorescence intensity per *z* plane for both WF and HiLo is plotted as a function of the distance from the focal plane. Theoretical axial response is plotted using Eq. (1). [Color figure can be viewed in the online issue, which is available at wileyonlinelibrary.com.]

NIH-PA Author Manuscript

NIH-PA Author Manuscript

NIH-PA Author Manuscript

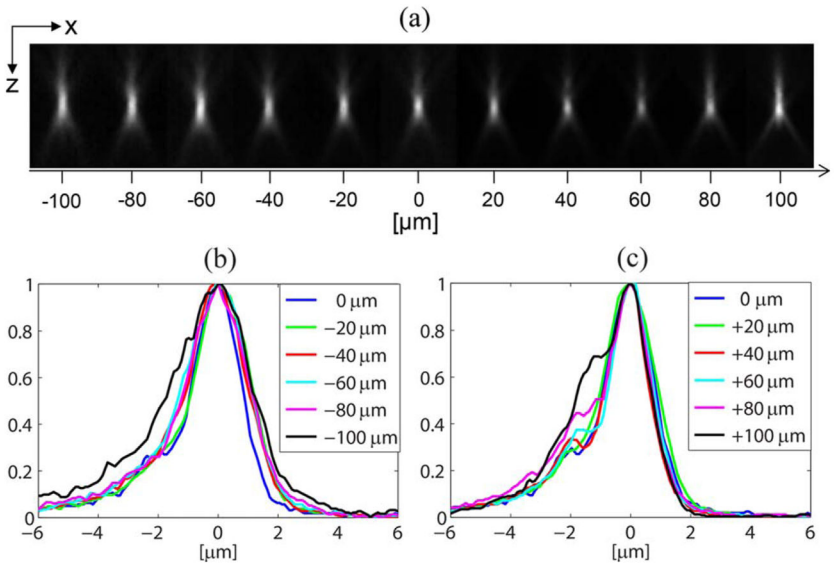

Figure 4.

PSFs of the remote focusing system. PSF is measured with 0.5 μm fluorescent beads at different depth near the focal plane of the imaging objective (OBJ). (**a**) *xz* sectional plot. (**b**) Normalized intensity plot along *z* for the negative direction (the objective moving closer to the bead). (**c**) Normalized intensity plot along *z* for the positive direction (the objective moving away from the bead). [Color figure can be viewed in the online issue, which is available at wileyonlinelibrary.com.]

NIH-PA Author Manuscript

NIH-PA Author Manuscript

NIH-PA Author Manuscript

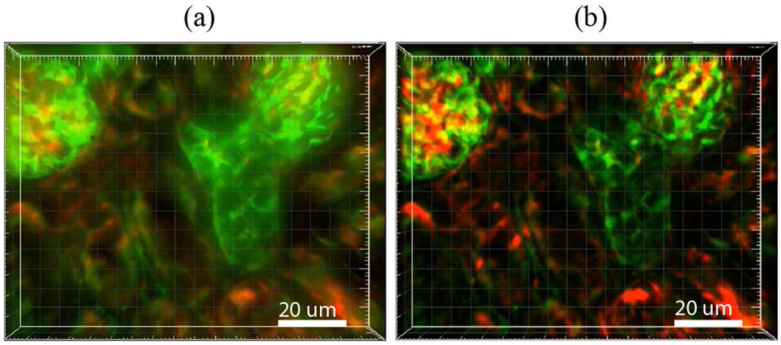

Figure 5.

3D image stack of mouse kidney obtained with (**a**) uniform illumination and (**b**) after HiLo processing. Green color represents elements of the glomeruli and convoluted tubules labeled with Alexa Fluor® 488 wheat germ agglutinin. Red color represents the filamentous actin prevalent in glomeruli and the brush border labeled with red-fluorescent Alexa Fluor 568 phalloidin. Forty slices of z-stack images are acquired at 0.5 μm z-step size with 20 msec exposure time per z-section. Image stack is generated from a central portion of full field of view to better visualize the background rejection effect. [Color figure can be viewed in the online issue, which is available at wileyonlinelibrary.com.]

NIH-PA Author Manuscript

NIH-PA Author Manuscript

NIH-PA Author Manuscript

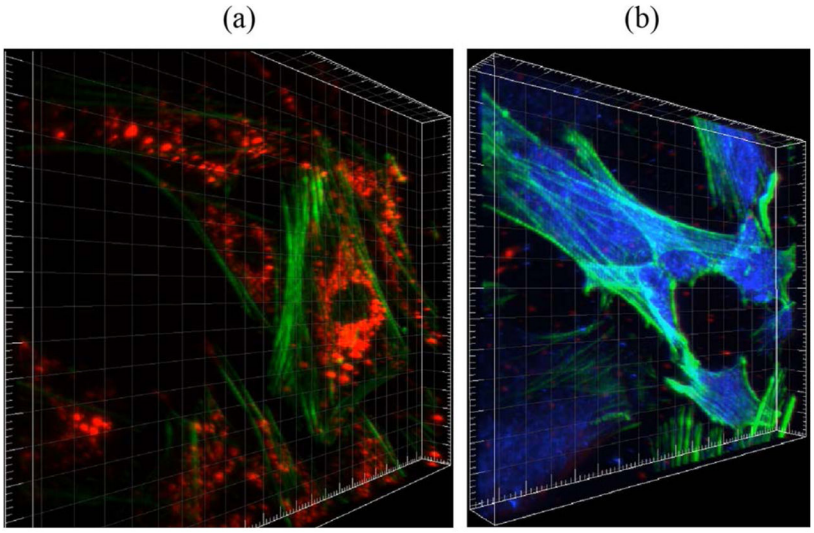

Figure 6.

(**a**) 3D image of the muntjac skin fibroblast cells (F36925, Invitrogen). The green color represents filamentous actin labeled with green fluorescent Alexa Fluor 488 phalloidin. The red color represents mitochondria labeled with an anti-OxPhos Complex V inhibitor protein mouse monoclonal antibody in conjunction with orange fluorescent Alexa Fluor 555 goat anti-mouse IgG. (**b**) TGFβ activated fibro-blast cells. Green color represents actin filament labeled with rhodamine phalloidin and blue color represents SMAD protein labeled with Alexa Fluor 488. 40 slices of z-stack images are acquired at 0.5 μm z-step size with 20 msec exposure time per z-section. Image stack is generated from a central portion of full field of view to better visualize the detailed structure of the cellular organelles. [Color figure can be viewed in the online issue, which is available at wileyonlinelibrary.com.]

NIH-PA Author Manuscript

NIH-PA Author Manuscript

NIH-PA Author Manuscript

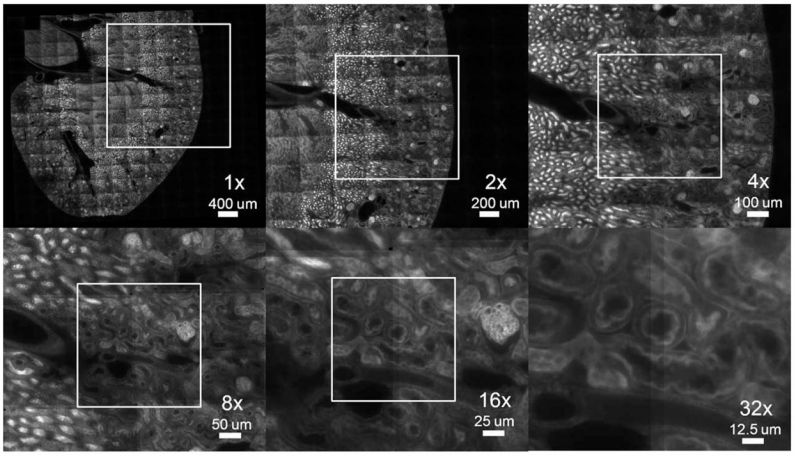

Figure 7.

Multiscale view of mouse kidney. 1× image is stitched with 16 × 16 FOVs where a FOV is 420 μm × 350 μm. Area marked with white square is zoomed in successively.

NIH-PA Author Manuscript

NIH-PA Author Manuscript

NIH-PA Author Manuscript

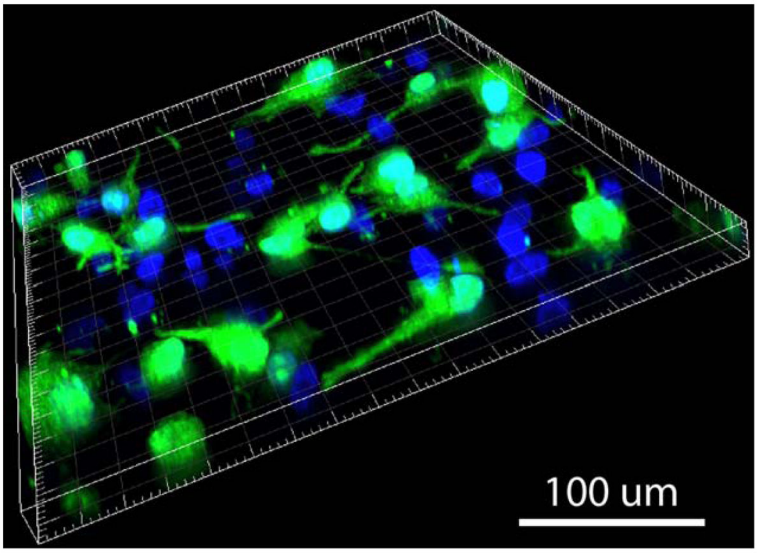

Figure 8.

Representative 3D image of rare cell sample at 1:1 mixing ratio. Cells with only mCherry label only appear as blue nuclei and the other cells with both mCherry and Cell Tracker Green labels appear as blue nuclei in green cell bodies. [Color figure can be viewed in the online issue, which is available at wileyonlinelibrary.com.]

NIH-PA Author Manuscript

NIH-PA Author Manuscript

NIH-PA Author Manuscript

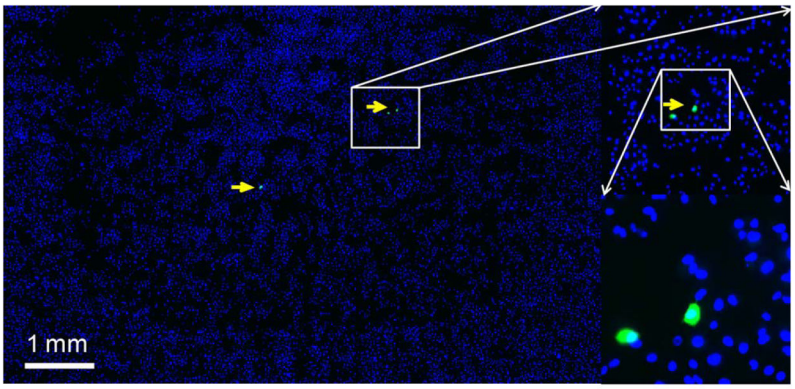

Figure 9.

Representative image of 1:10^4 ratio sample where the nucleus is labeled with m-Cherry (represented as blue color) and the cytoplasm is labeled with Cell Tracker Green (represented as green color). The size of single FOV is 420 μm × 350 μm and the image shown is part of the 1:10^4 ratio sample where 20 × 15 FOVs are stitched together. [Color figure can be viewed in the online issue, which is available at wileyonlinelibrary.com.]

NIH-PA Author Manuscript

NIH-PA Author Manuscript

NIH-PA Author Manuscript

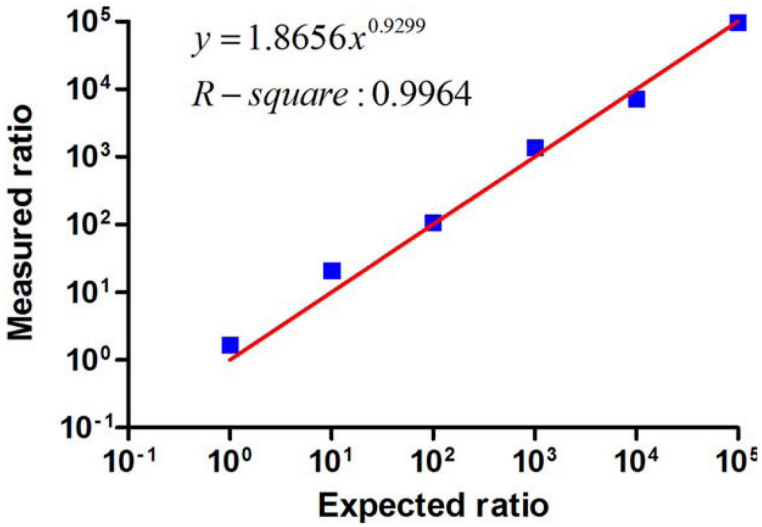

Figure 10.

Rare cell subpopulation counting result with various mixture ratios from 1:1 down to $1:10^5$. Measured ratio (in *y*-axis) is plotted against the expected ratio (in *x*-axis). [Color figure can be viewed in the online issue, which is available at wileyonlinelibrary.com.]